Nanoscale

PAPER

View Article Online
View Journal | View Issue

Cite this: *Nanoscale*, 2014, **6**, 9655

High-performance all-solid-state flexible micro-supercapacitor arrays with layer-by-layer assembled MWNT/MnO_x nanocomposite electrodes†

Geumbee Lee,[a] Daeil Kim,[b] Junyeong Yun,[b] Yongmin Ko,[b] Jinhan Cho[b] and Jeong Sook Ha*[ab]

Received 15th April 2014
Accepted 1st June 2014

DOI: 10.1039/c4nr02035a

www.rsc.org/nanoscale

In this study, we report on the fabrication of high performance planar-type flexible micro-supercapacitor (MSC) arrays using Au electrodes coated with a functionalized multi-walled carbon nanotube (MWNT) film and a layer of MWNT-COOH/MnO_x nanoparticle (NP) composite on top. The MWNT thin film was formed *via* layer-by-layer (LbL) assembly of MWNTs functionalized with amine groups and MWNTs with carboxylic acid groups in water. The hydrothermally synthesized composite of MWNT-COOH/MnO_x NPs was coated on top of the MWNT film (LbL-MWNT). The addition of MWNT-COOH/MnO_x NP composite as a top layer enhanced the performance of the MSCs dramatically, resulting in a volumetric capacitance of 50 F cm^{-3} at a scan rate of 10 mV s^{-1} and a coulombic efficiency of ~100%. By contrast, a volumetric capacitance of 3.6 F cm^{-3} was obtained when using only the LbL-MWNT film. After repetitive operation up to ~10^4 times, the capacitance remained at ~88.3% of the original value. With a deliberate circuit design consisting of serially connected MSC arrays, various light-emitting diodes operating at different bias voltages could be lit. The MSC circuit fabricated on a polyethylene terephthalate (PET) film showed stable electrochemical properties upon 1000 cycles of bending deformation.

1. Introduction

According to the increasing interest in portable and wearable electronic devices, the need for flexible and light energy-storage equipment has gradually increased.[1–4] Among various energy-storage devices, electrochemical capacitors, also known as supercapacitors or ultracapacitors, have been spotlighted as next-generation energy-storage devices. Supercapacitors have a high power density due to fast charging and discharging rates, long cycle life, and excellent safety, compared to conventional batteries.[5–7]

Depending on the electrode materials and the charge-storage mechanism, supercapacitors can be classified into two types: electrochemical double layer capacitors (EDLCs) and pseudocapacitors.

In EDLCs, an electrical double layer is formed at the interface of the electrode and the electrolyte *via* ionic charge separation of the electrolyte. In this case, carbon-based materials, such as activated carbon, carbon nanotubes, graphene, carbon black, or carbon aerogel are generally used as electrode materials.[8–12]

In pseudocapacitors, a fast redox reaction between the electrode surface and the electrolyte generates the high capacitance and energy density. Here, the electrode materials used include metal oxides or conducting polymers. Recently, metal oxides such as RuO_2, CuO, NiO, MnO_2, and IrO_2 were reported to contribute to the capacity increase of supercapacitors.[13–21] Even though the use of RuO_2 or IrO_2 resulted in high capacity, superior electrical conductivity, and chemical stability, their high price and toxicity limits their widespread application.[14,22] In contrast, manganese oxides seem to be an alternative in producing a high energy density in supercapacitors since they are cheap, environmentally friendly, abundant in nature, and have high theoretical specific capacities.[23–27]

If manganese oxide is used as an electrode material for supercapacitors, it is important to increase the surface area and electrical conductivity in order to achieve a high capacitance. Therefore, the combination of carbon nanotubes having a large surface area and excellent conductivity along with manganese oxide may represent a solution for high-performance supercapacitors.[28–31] To date, many groups have proved some improvement of the supercapacitor performance *via* the use of carbon-based materials/metal–oxide composite electrodes. It is also critical to prepare the electrode materials with uniform

[a]*KU-KIST Graduate School of Converging Science and Technology, Korea University, Seoul, 136-701, Republic of Korea. E-mail: jeongsha@korea.ac.kr*

[b]*Department of Chemical and Biological Engineering, Korea University, Seoul, 136-701, Republic of Korea*

† Electronic supplementary information (ESI) available. See DOI: 10.1039/c4nr02035a

thickness to ensure reproducible performance of the supercapacitors.

For the realization of portable nanoelectronic devices with embedded energy-storage devices, such as supercapacitors, it is necessary to integrate the supercapacitors into the circuit of the working device.[32] Therefore, it is advantageous to have a planar-type supercapacitor that is easier to be fabricated on the same device substrate *via* a lithography technique than conventionally produced, vertically stacked supercapacitors since planar types do not need to have a separator between two electrodes. In addition, the ion pathway becomes shorter due to the two-dimensional transport of ions in the electrolyte, and the thickness of the planar-type supercapacitor is smaller compared to the stacked one.[33] Furthermore, all-solid-state supercapacitors which do not use a liquid electrolyte can be directly implemented as embedded energy-storage devices of portable nanoelectronic systems.[34]

In this work, we fabricated flexible planar-type micro-supercapacitor (MSC) arrays by adopting the multi-walled carbon nanotube (MWNT) film with a top layer of the MWNT-COOH/MnO_x nanoparticle (NP) composite and the MWNT/MnO_x composite film, as an electrode material since MWNTs have a higher electrical conductivity than single-walled carbon nanotubes (SWNTs). In addition, we used the layer-by-layer assembly (LbL) method for forming the MWNT/MnO_x composite films since it is simple, cost-effective, and can be applied for large-area deposition of various materials. In particular, it is easy to control the thickness of the film at the nanometer scale.[35,36] MWNT-COOH/MnO_x nanocomposites synthesized by the hydrothermal method were deposited on the LbL-MWNT film to form a supercapacitor electrode. Such formed porous 3D network electrode structures in the supercapacitors generated a high capacitance and energy density through effective diffusion of the electrolyte and fast electronic and ionic conduction.[28]

The performance of the supercapacitors strongly depends on the whole structure of the electrodes and the electrolyte as well as the electrode materials and its fabrication method. We made an LbL assembled MWNT/MnO_x supercapacitor, having a planar-type patterned electrode with micro-channels for ionic conduction *via* the photo-lithography technique and used the gel-type electrolyte of PVA–H_3PO_4. Furthermore, by designing planar-type MSC arrays, we controlled the total capacitance and the output voltage of such fabricated micro-supercapacitors by fabricating a circuit of micro-supercapacitor arrays. Through this, we could light various μ-LEDs with different operating voltages. The stable performance of the fabricated MSC arrays if subjected to mechanical deformation, namely bending, also demonstrates the high application potential in future portable devices.

2. Experimental procedures

Functionalization of negatively and positively charged MWNTs

To functionalize MWNTs with negatively charged carboxyl groups, 500 mg of MWNTs (Aldrich, >95% purity, length 5 μm, outer diameter 6–9 nm) were refluxed in a mixed solution of sulfuric acid and nitric acid (with volume ratio of 3 : 1, Sigma-Aldrich) at 70 °C for 3 h. Then, vacuum filtration and rinsing with deionized water (DI-water) through a mixed cellulose ester membrane filter (ADVANTEC MFS, Inc., pore size 0.2 μm, diameter 47 mm) was carried out several times. After osmosis filtration using a tube cellulose membrane (Sigma, avg. flat width 33 mm, avg. diam. 21 mm), negatively charged MWNTs (MWNT-COO^-) were finally obtained.

Positively charged MWNTs (MWNT-NH_3^+) were obtained by adding ethylenediamine ($NH_2(CH_2)_2NH_2$, Sigma-Aldrich) and 1-ethyl-3-(3-dimethylaminopropyl)carbodiimide (EDC, Aldrich) into an aqueous solution of MWNT-COOH while stirring at room temperature for 5 h.

Synthesis of MWNT-COOH/MnO_x nanocomposites

MWNT-COOH/MnO_x nanocomposites were synthesized by the hydrothermal method. MWNT-COOH dispersed in 30 mL of absolute ethanol and 100 mg of manganese(II) acetate tetrahydrate ($Mn(CH_3COO)_2 \cdot 4H_2O$, Aldrich) were put in a Teflon bottle and subjected to high pressure by using a tightly locked autoclave. The autoclave was maintained at 150 °C for 3 h in an oven. After cooling to room temperature within a day, the black product was rinsed several times with DI-water using a mixed cellulose ester membrane filter. After drying filtered composites and peeling them off from the membrane filter, MWNT-COOH/MnO_x nanocomposites could be obtained.

Fabrication of patterned all-solid-state micro-supercapacitors

The fabricated planar-type all-solid-state MSC consists of a 3 × 3 array of MSCs which were patterned on a SiO_2/Si wafer by photolithography using a AZ5214 photo resist. A Ti/Au (5/50 nm) film deposited by electron-beam evaporation was patterned by photolithography to be worked as a current collector, which improves the electrical contact with the active materials. The electrodes were fabricated by LbL of functionalized MWNTs. After dipping a SiO_2/Si substrate with Au patterns in a solution of positively charged MWNTs (MWNT-NH_3^+) for 10 min, it was rinsed for 1 min to remove weakly adsorbed MWNTs. Then, the same process was repeated using negatively charged MWNTs (MWNT-COO^-). After repeating this cycle 19 times, MWNT-NH_3^+ was coated once again.

The MWNT-COOH/MnO_x composites synthesized by the hydrothermal reaction were dispersed in deionized water and the substrate with the LbL-assembled MWNT film was dipped into this solution for 10 min, resulting in a multilayer of MWNT films and an additional final layer of MWNT-COOH/MnO_x. Then, the residual film except for the patterned area was removed *via* the lift-off process. The photograph of such a planar-type MSC array is shown in the ESI Fig. S1.† The channel length of the MSCs is patterned to be 150 μm *via* the photolithography technique. Even though the small channel length would result in higher capacitance, we tuned it to 150 μm considering the technical difficulty in the lift-off process.

Since the array consists of 9 MSCs, where each MSC has an area of 1.73 mm^2 including the channel length of 150 μm, the total area of the MSC arrays is estimated to be 15.5 mm^2.

For synthesizing polyvinyl alcohol (PVA, Aldrich, MW 89 000–96 000)–phosphoric acid (H_3PO_4, Sigma) gel electrolyte, 15.0 mL of H_3PO_4 was added to 150 mL of deionized water and 15.0 g of PVA was mixed under strong stirring at 150 °C. When the electrolyte solution became transparent and changed to a gel state, it was drop-cast onto the electrode surface. After the PVA–H_3PO_4 gel electrolyte was solidified, the fabrication of the planar-type all-solid-state MSC was completed.

Characterization

The chemical composition of MWNT-COOH/MnO_x was analyzed using X-ray photoelectron spectroscopy (XPS, ULVAC-PHIX-Tool) and X-ray diffraction (XRD, Philips, X'Pert PW3040/00) operated at 40 kV and 30 mA with Cu Ka radiation. In order to check that the thickness of LbL assembled MWNT films depending on the number of uniformly controlled layers, UV-visible spectroscopy was carried out (UV-vis spectrometer, Perkin-Elmer Lambda 35). Scanning electron microscopy (SEM, Hitachi S-4800) and transmission electron microscopy (TEM, FEI TECNAI) were performed to observe the morphology and structure of the electrode materials. Photographic images were obtained using a Samsung Galaxy Note II and a Canon Eos 7D. The electrochemical properties were measured by means of cyclic voltammetry (CV), galvanostatic charge–discharge, and electrochemical impedance spectroscopy (EIS) using an electrochemical analyzer (Ivium Technologies, Compact Stat). EIS was investigated in the frequency range from 1 MHz to 100 mHz at a potential amplitude of 10 mV. The specifications of μ-LEDs (ROHM comp. China) used to evaluate the charge–discharge performance of the MSC arrays are 3.3 V, 20 mA (blue light), 2.2 V, 20 mA (green light), 2.0 V, 20 mA (yellow light), and 1.8 V, 20 mA (red light), respectively. The mechanical stability with respect to bending of the flexible MSCs was tested by using a homemade bending stage.

3. Results and discussion

Scheme 1 shows the whole fabrication process of the planar-type MSC arrays. The LbL-MWNT nanocomposite multilayer films (MWNT-NH_3^+/MWNT-COO^-)$_n$ were prepared by successive adsorption of MWNT-NH_3^+ and MWNT-COO^- on a gold-patterned substrate *via* electrostatic attraction.[37] After repeating 19 cycles, MWNT-NH_3^+ was coated once again. Finally an additional top layer of MWNT-COO^-/MnO_x nanocomposites was adsorbed on the (MWNT-NH_3^+/MWNT-COO^-)$_n$ film. For the patterned LbL deposition of MWNT thin films on Ti/Au metal electrodes, the photolithography technique was used. The lift-off resist (LOR) and photo resist (PR) were deposited on an Au patterned substrate *via* spin coating. And then UV was irradiated to the LOR and PR coated substrates using a photo-mask so that the UV-exposed LOR and PR areas could be removed by the developer. We deposited functionalized MWNTs on that resultant substrate *via* the LbL assembly technique. Finally, the substrate coated with MWNT films was dipped into acetone and developer so that the LOR and PR were lifted off with residual MWNT films. Therefore, LbL assembled MWNT films on the substrate were removed except for the electrode region and the active materials were not adsorbed on the channel. More detailed processing steps can be found in the ESI† of our previous work.[38]

The lower part of Scheme 1 is a cross-sectional view of a planar-type MSC, which clearly shows the structure of all-solid-state MSCs fabricated in such a way using the gel electrolyte.

For the quantitative analysis of the multilayer structures, UV-visible absorption spectra are shown in Fig. 1(a). When positively charged MWNTs and negatively charged MWNTs were alternatively adsorbed on the quartz substrate, absorbance maximum at ~250 nm increased in proportion to the number of layers (inset of Fig. 1(a)). It qualitatively shows that the amount of adsorbed MWNT/layer is uniform. Based on these results, thickness per layer can be quantitatively obtained by dividing the total film thickness by the total number of layers.[39] In the previous work,[37] it was shown that the performance of the supercapacitor was strongly dependent on the thickness of the film. In order to confirm that, we measured the capacitance of MSCs with different thicknesses of LbL films. Total capacitance increased with the number of MWNT bilayers. However, the volumetric capacitance remained almost the same for 10, 15, and 20 bilayer films as shown in the ESI Fig. S2.† The slight increase observed in the MSC with 20 bilayer films is attributed to the enhanced conductivity.

The SEM image taken from the thin-film electrode consisting of 20 LbL-MWNT/MnO_x (a film of 19 LbL-MWNTs and 1 layer of MWNT-COO^-/MnO_x) is shown in Fig. 1(b) and the corresponding cross-sectional image is also shown in the inset with the scale bar corresponding to 200 nm. A uniformly formed LbL-MWNT/MnO_x film is ascertained with a thickness of 300 nm over a large area. The thicknesses of the 20 LbL films of MWNT and MWNT/MnO_x were compared by taking cross-sectional SEM images as shown in the ESI Fig. S3.† Since only the top-most layer of MWNT/MnO_x is deposited with a very small amount of MnO_x particles as observed in the TEM image of Fig. 2(a), we prepared thicker films of 20 LbL assembled layers with positively charged solution of MWNT-NH_3^+ under a lower pH of 5.8 than that used for the preparation of the 300 nm thick film (Fig. 1(b)).[37] As shown in the SEM images, both films showed a thickness of 500 nm without any noticeable difference. TEM measurements were performed to investigate the distribution and morphology of the MnO_x particles on the MWNT-COOH/MnO_x composites (Fig. 2(a)). As shown in the TEM image, particles with a size of a few tens of a nm exist on entangled MWNT-COOH. In order to analyze the chemical composition of those nanostructures, energy dispersion spectroscopy (EDS) measurements were performed in two different areas: the blue-squared area of functionalized MWNT (MWNT-COOH) and the red-squared area of MnO_x NPs on the MWNT-COOH. As distinguished by the two EDS spectra of Fig. 2(b), Mn peaks and an O peak of higher intensity are observed in the red-squared area, in addition to the C and O peaks likewise observed in the blue-squared area. These findings confirm that

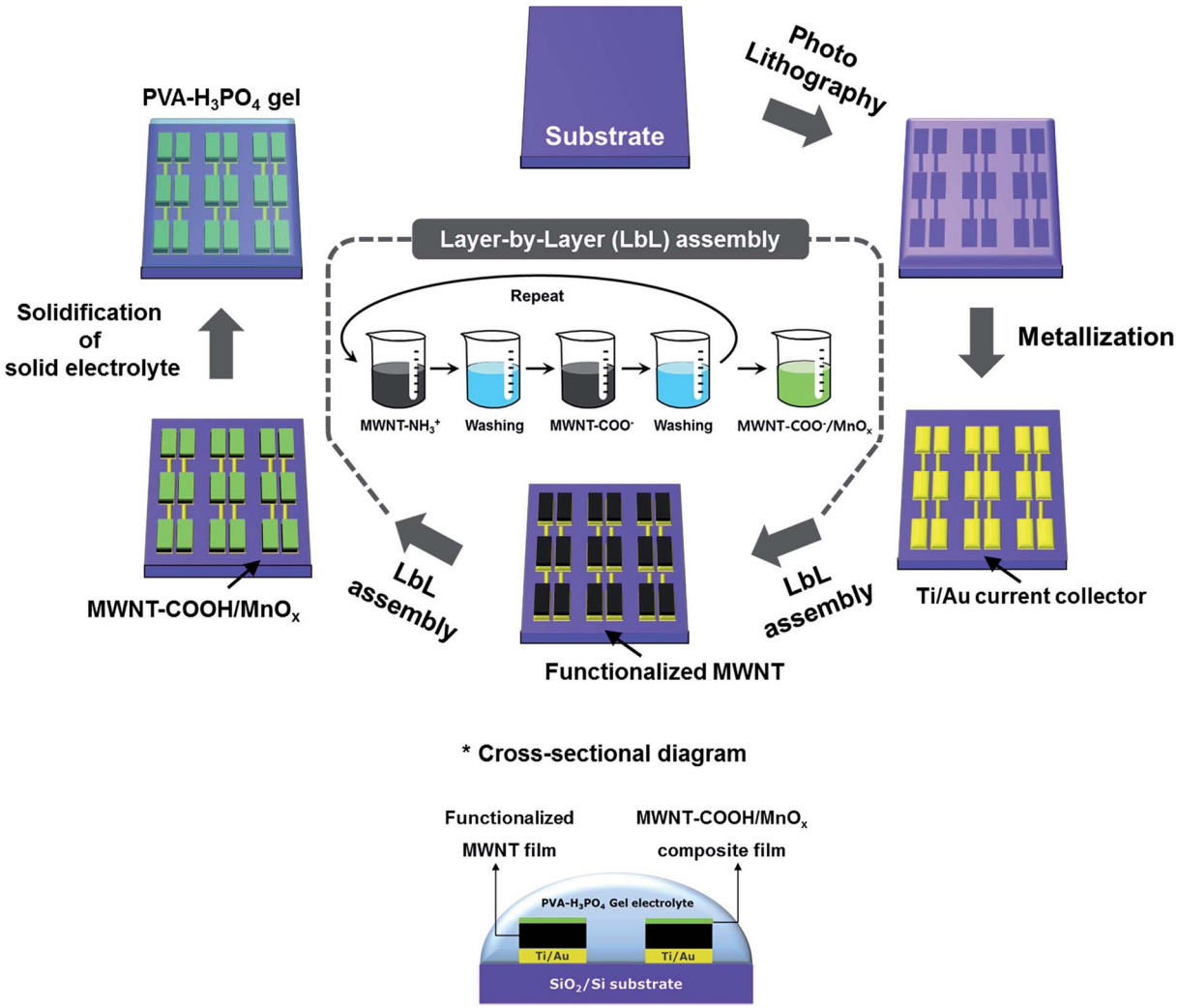

Scheme 1 Schematic illustration of the fabrication process of a planar-type MSC array. The bottom figure shows a cross-sectional diagram of a planar-type MSC. Here, the interconnections between the MSCs are presented as simple straight lines but actual shapes are curved ones given in the ESI Fig. S1.†

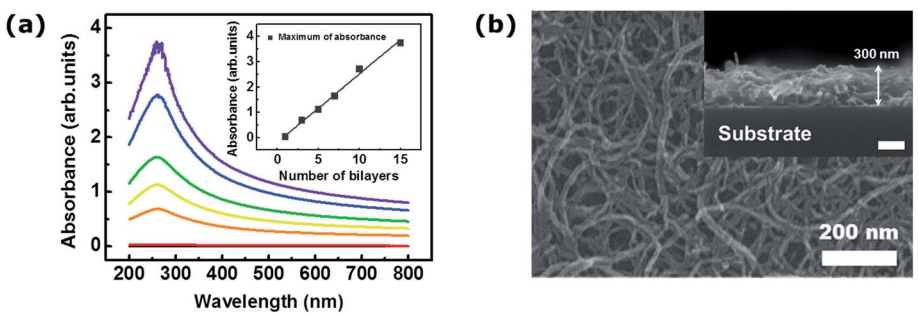

Fig. 1 (a) UV-visible absorption spectra of LbL-assembled MWNT thin films. (b) SEM image of the LbL-MWNT/MnO_x electrode. The inset is the cross-sectional SEM image of the LbL-MWNT/MnO_x electrode with a scale bar of 200 nm.

the NPs are composed of manganese oxide. The Cu peak originates from the used TEM grid. In order to determine the specific oxidation state of manganese, XPS measurements were performed. The oxidation state of manganese can be determined more reliably by observing the splitting of the Mn 3s peak (Fig. 2(c)). Such a splitting of the Mn 3s peak occurs due to the interaction between the 3s orbital and the other electrons.[40,41] The splitting interval is 6.0 eV, implying that the chemical formula of MnO_x is either MnO or Mn_3O_4.[41,42] Meanwhile, as shown in the inset of Fig. 2(c), the Mn 2p spectrum has

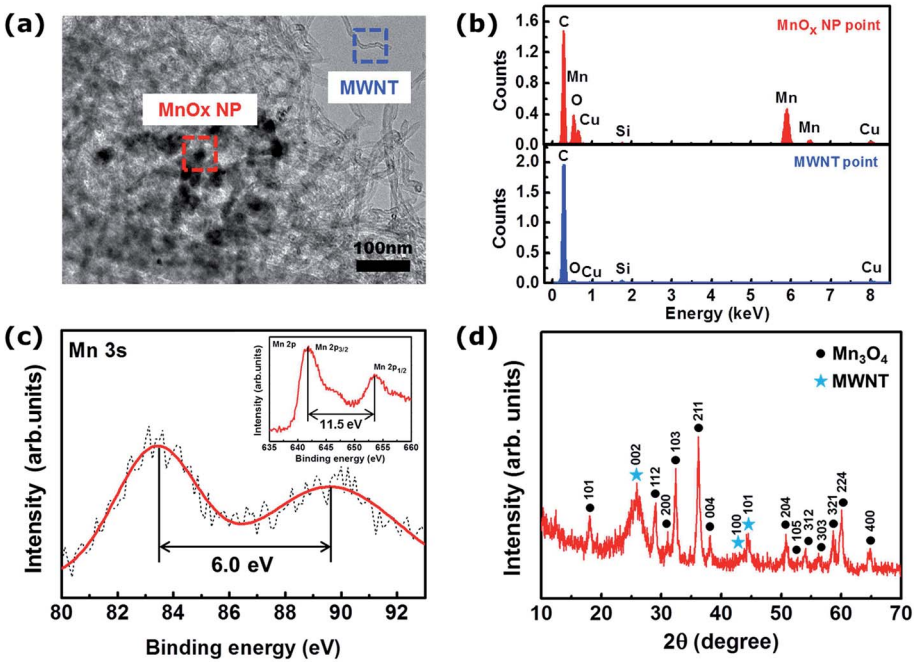

Fig. 2 (a) TEM image of MWNT-COOH/MnO_x nanocomposites synthesized by the hydrothermal method. The red and blue squares indicate MnO_x nanoparticles and MWNT-COOH, respectively. (b) EDS spectra taken from the red (top) and the blue (bottom) squared area of the TEM image, respectively. (c) Enlarged XPS spectra of the Mn 3s region of the MWNT-COOH/MnO_x nanocomposites and Mn 2p (inset) peaks. (d) XRD spectrum taken from MWNT-COOH/MnO_x nanocomposites.

two sharp peaks at binding energies of 641.9 eV and 653.4 eV, corresponding to Mn $2p_{3/2}$ and Mn $2p_{1/2}$, respectively. This splitting interval is 11.5 eV, which is similar to the value previously reported for Mn_3O_4.[41,42] Based on the values of the Mn 3s and Mn 2p peak splitting, we tentatively consider most of the MnO_x compounds synthesized in this work to be Mn_3O_4. The X-ray diffraction (XRD) spectrum taken from the MWNT-COOH/MnO_x powder shows the diffraction peaks typically observed in Mn_3O_4 in Fig. 2(d). The presence of Mn_3O_4 was determined by characteristic diffraction peaks. In the XRD pattern, the diffraction peaks at 18.1, 28.9, 31.0, 32.4, 36.2, and 38.0° are well-assigned to the (101), (112), (200), (103), (211) and (004) plane, respectively and demonstrate that hausmannite Mn_3O_4 has a tetragonal structure.[27] From those peaks, lattice constants are estimated to be $a = b = 5.765$ and $c = 9.442$ Å, indicating the standard values of bulk Mn_3O_4 (JCPDS card, file no. 24-0734). Additional peaks shown in the XRD pattern signify the existence of MWNTs. Also, synthesized manganese oxide is considered to have an excellent crystalline quality because there is no obvious impurity peak.

Therefore, we consider that the MnO_x particles synthesized in this work are Mn_3O_4.

ESI Fig. S4† shows a survey spectrum of the MWNT-COOH/MnO_x nanocomposites taken over the binding-energy range from 0 to 1000 eV in which the C, Mn, and O peaks are observed.

In Fig. 3, cyclic voltammetry (CV), galvanostatic charge–discharge, and electrochemical impedance spectroscopy (EIS) measurements are presented for a comparison of LbL-MWNT MSC and LbL-MWNT/MnO_x MSC. The CV curves were taken at a scan rate of 500 mV s^{-1} using the PVA–H_3PO_4 gel electrolyte (Fig. 3(a)). The volumetric capacitance (C_U) of an MSC can be obtained by the following equations.

$$C = \frac{2\int_{V_i}^{V_f} (I \cdot V)\mathrm{d}V}{S \cdot (V_f - V_i)} \quad (1)$$

$$C_U = \frac{C}{U} \quad (2)$$

C is the total capacitance, $\int_{V_i}^{V_f} (I \cdot V)\mathrm{d}V$ is the CV curve area, $(V_f - V_i)$ is the potential window, and U is the volume of the active materials and the current collector. Considering the array of 3 × 3 MSCs, the total volume is estimated to be 5.50×10^{-6} cm^3, where the thickness of the electrode, 355 nm, including the Ti/Au film and the LbL-MWNT/MnO_x film is used and the active area of 0.155 cm^2 includes the electrodes and the channel. Since the total capacitance C is proportional to the CV curve area, it is clearly shown that the capacitance of LbL-MWNT/MnO_x MSC is larger than that of LbL-MWNT MSC. The much higher capacitance of LbL-MWNT/MnO_x MSC is attributed to the pseudo capacitive property of MnO_x NPs resulting from the redox reaction that additionally contributes to the electrical double-layer capacitance of LbL-MWNT MSC, although the 3D porous structures created by the LbL assembly method also contribute to the higher capacitance by enabling an effective diffusion of the electrolyte. As a result, the ultrathin-film electrode based on LbL-MWNT/MnO_x nanocomposites significantly improves the volumetric capacitance. Even though

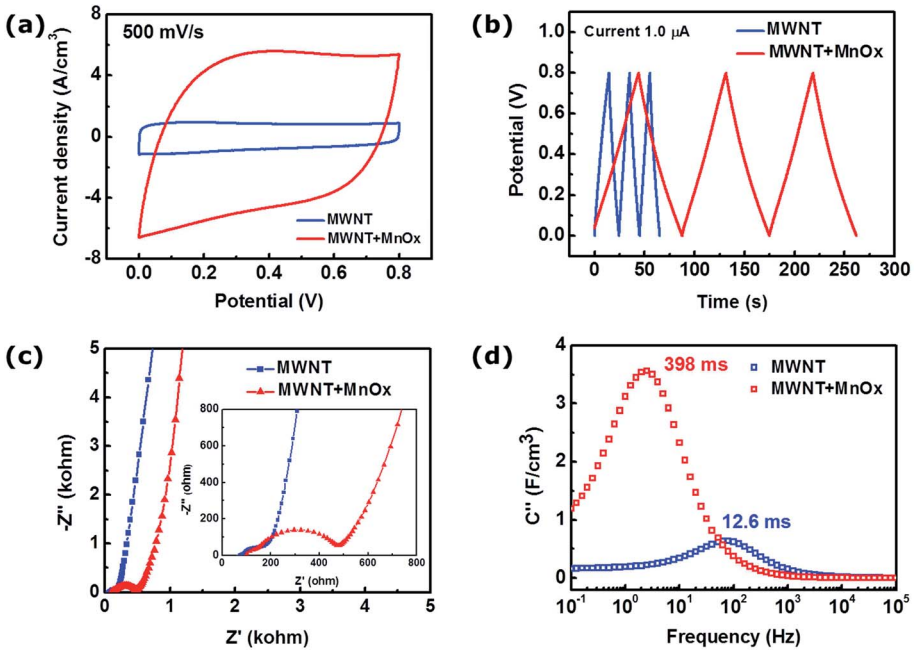

Fig. 3 Electrochemical properties of LbL-MWNTs (blue) and LbL-MWNT/MnO_x (red) MSCs. (a) CV curves at a scan rate of 500 mV s^{-1}. (b) Galvanostatic charge–discharge curves at a current of 1.0 μA. (c) Nyquist plots. The inset shows the high-frequency region in more detail. (d) The imaginary part of the capacitance (C'') as a function of frequency.

the redox peaks due to MnO_x particles were expected to be observed at low scan rates, there appeared no clear peaks related to the redox reaction in the CV curves. Such behavior was explained in several studies by others as follows: the electrode materials based on MnO_x can be stabilized by using the PVA–H_3PO_4 gel electrolyte[33] or the synthesized composite electrode itself is stable enough to exhibit capacitive behaviors.[43] However, we cannot clearly give an explanation on our result at this moment.

Fig. 3(b) shows galvanostatic charge–discharge curves measured in the stable voltage range from 0.0 to 0.8 V by applying a constant current of 1.0 μA. The voltage *vs.* time profile of each curve tends to be linear and the charging and discharging profiles seem to be symmetric without any significant voltage drop. The discharging time of the LbL-MWNT/MnO_x MSC is about four times longer than that of the LbL-MWNT MSC, which also supports the experimentally observed result that LbL-MWNT/MnO_x MSC has a higher capacitance than LbL-MWNT MSC.

For further confirming the improved performance of LbL-MWNT/MnO_x MSC, EIS measurements were performed in the frequency range from 1 MHz to 100 mHz. As evident from the corresponding Nyquist plots shown in Fig. 3(c), at high frequency, MSCs act like a resistor while they show capacitive behavior toward lower frequency.[44] The measured resistance is the sum of various contributions, such as the electronic resistance of the active material, the contact resistance between the current collector and the active material, the internal resistance of the metal oxide, and the electrolyte resistance of the porous structure of the electrode.[45] During operation of the supercapacitor, the resistance can be significantly increased, depending on frequency. For example, the Nyquist plot is almost parallel to the imaginary part ($-Z''$-axis) and such a vertical line indicates that the real part (Z'-axis) almost does not change with frequency.[44] Therefore, these results clearly demonstrate a stable performance of both fabricated MSCs. From the enlarged Nyquist plots shown in the inset, the equivalent-series resistance (ESR) values of LbL-MWNTs and LbL-MWNT/MnO_x MSCs are estimated to be 73 Ω and 102 Ω, respectively. The slightly higher ESR value of LbL-MWNT/MnO_x MSC is probably due to the internal resistance of manganese oxide.[46]

To more clearly understand the device performance of the two different MSCs, the imaginary part of the capacitance $C''(\omega)$ was evaluated as a function of frequency ω, as shown in Fig. 3(d). ω is calculated by the equation $\omega = f2\pi$. $C''(\omega)$ corresponds to energy losses by irreversible processes and is defined as follows:

$$C''(\omega) = \frac{Z'(\omega)}{\omega |Z(\omega)|^2} \quad (3)$$

The response frequency f_0, corresponding to the maximum point of the energy curve, was estimated to be 79.4 Hz and 2.51 Hz for LbL-MWNT and LbL-MWNT/MnO_x MSCs, respectively. Therefore, the relaxation-time constant τ_0 is calculated to be 12.6 ms and 398 ms for LbL-MWNTs and LbL-MWNT/MnO_x MSCs, respectively, by using the relationship of $\tau_0 = 1/f_0$. The relaxation time is the minimum time required to discharge the stored energy of a supercapacitor. Thus, a small value of τ_0 indicates that supercapacitors have ability for instantaneous

high power.[44,47] The present values are much smaller than previously reported ones.[48–50]

Fig. 4 summarizes the electrochemical properties of LbL-MWNT/MnO_x MSCs. CV curves at various scan rates (10 mV s^{-1}, 20 mV s^{-1}, 50 mV s^{-1}, 100 mV s^{-1}, 150 mV s^{-1}, 200 mV s^{-1}, 300 mV s^{-1}, and 500 mV s^{-1}) are shown in Fig. 4(a). The CV curves are almost rectangular and maintained their shape even at high scan rates. The maximum volumetric capacitance is estimated to be 50 F cm^{-3} at a scan rate of 10 mV s^{-1}. The specific volumetric capacitance of LbL-MWNT/MnO_x MSCs depending on the scan rate is presented in the ESI Fig. S5.† The discharging current and the scan rate show a linear relationship up to a scan rate of 5 V s^{-1}, which certainly indicates the high power of the fabricated LbL-MWNT/MnO_x MSC.[48,50–52] In this work, loading of MnO_x nanoparticles would be a key factor for the performance of specific capacitance. In order to understand the effect of loading of MnO_x nanoparticles on the performance of the supercapacitor arrays, we synthesized the nanocomposites of MWNT-COOH/MnO_x with 5 different mass ratios of MWNT-COOH and $Mn(CH_3COO)_2 \cdot 4H_2O$ at 150 °C for 3 h; mass ratios are 2 : 1, 1 : 3, 1 : 5, 1 : 7, and 1 : 10. We fabricated the 5 MSCs with different MnO_x loadings and measured their CV curves at a scan rate of 500 mV s^{-1}. As shown in the ESI Fig. S6,† the specific capacitance had a strong dependence on the mass ratio. Compared to the mass ratio of 1 : 5, which is the maximum value of C/C_0 in this work, the specific capacitance was much lower for the mass ratio of 2 : 1 and a little bit lower for that of 1 : 3, 1 : 7 and 1 : 10. With the small content of MnO_x, an insufficient redox reaction should have occurred at the interface between the electrolyte and the electrode materials, while excess loading of MnO_x could increase the internal resistance to reduce the capacitance. In conclusion, we consider that there should exist the optimum mass loading of MnO_x for the best performance. In recent studies, it was also demonstrated that the device performance changed with mass loading of pseudo capacitive materials in the similar way.[53,54]

Since the distribution of MnO_x NPs does not seem to be uniform over the whole film area, we checked the reproducibility of the device performance by taking 5 different MSC devices and the variation of the capacitance is marked as error bars in the ESI Fig. S7.† The standard deviation of MSC capacitance is about ±6.7, which is almost independent of the scan rate.

Fig. 4(b) shows the galvanostatic charge–discharge curves of LbL-MWNT/MnO_x MSCs. The voltage *vs.* time profile is linear, irrespective of the current varying in the range from 0.5 to 10 μA and the curves maintain their symmetric, triangular shape. Charging and discharging time are approximately the same suggesting the coulombic efficiency to be ~100%. In addition, no sudden voltage drop was observed, signifying that the LbL-MWNT/MnO_x MSC worked stably.

In the case of pseudocapacitors, repeated redox reactions can result in a degradation of the metal oxides. Therefore, a long cycle life is an important factor to evaluate the performance of supercapacitors. After repeating charge–discharge cycles for 10 000 times at a current of 5.0 μA, the capacity retention is measured to be about 88.2%. Furthermore, the charge and discharge curves after almost 10 000 cycles did not show a change in their symmetric, triangular shape, as demonstrated in the inset of Fig. 4(c).

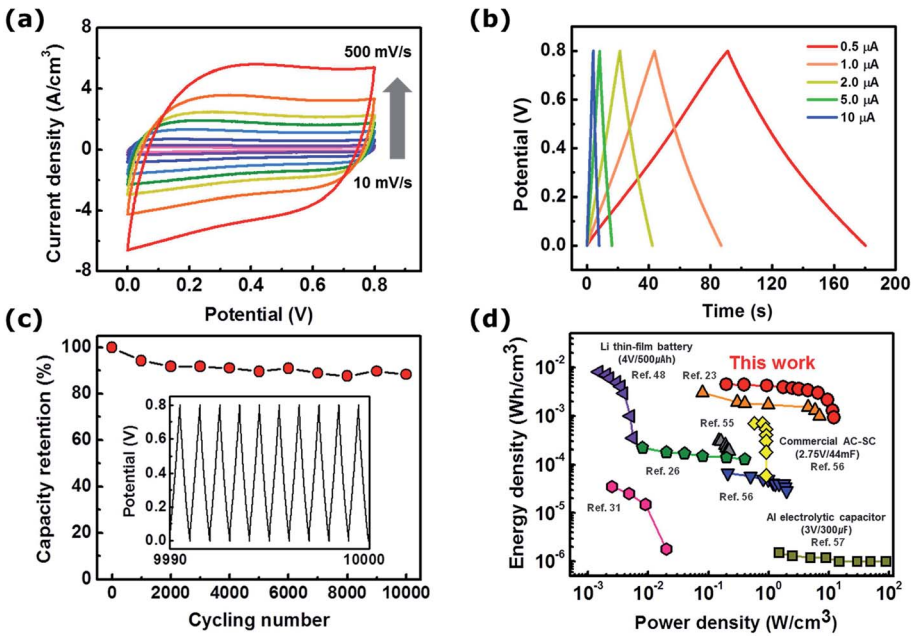

Fig. 4 Electrochemical properties of LbL-MWNT/MnO_x MSCs. (a) CV curves at different scan rates varying from 10 to 500 mV s^{-1}. (b) Galvanostatic charge–discharge curves at different currents from 0.5 to 10 μA. (c) The capacity retention as a function of the cycling number: the inset shows the shape of the charge–discharge curves near 10 000 cycles. (d) Ragone plots providing a comparison with other energy-storage devices.

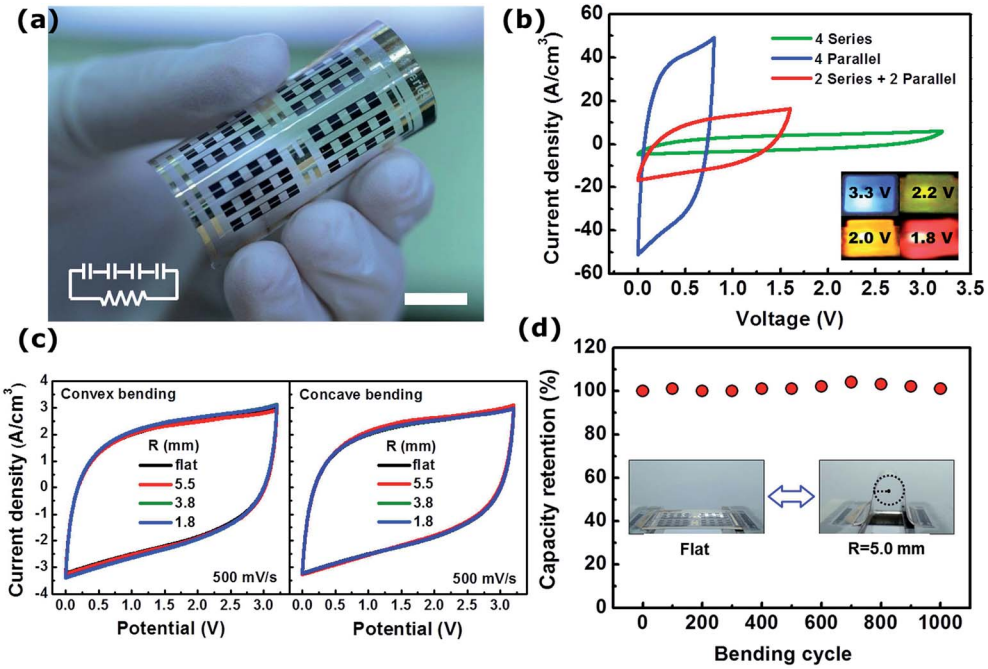

Fig. 5 (a) Photograph of 4 LbL-MWNT/MnO_x MSC arrays connected in series on a PET substrate. The inset shows the circuit diagram. The scale bar corresponds to 1 cm. (b) CV curves of 4 MSC arrays in series, in parallel, and 2 in series and 2 in parallel. The inset shows LEDs operated by the MSC circuits at various output voltages. (c) CV curves of flexible an MSC circuit with different bending radii. (d) Capacity retention as a function of the bending cycle number. The inset shows photographs of the flat and bent MSC circuits.

Ragone plots of LbL-MWNT/MnO_x MSCs and other energy-storage devices are presented in Fig. 4(d). The volumetric energy density E and power density P are calculated by the following equations.

$$E = \frac{C_U \cdot (\Delta V)^2}{7200} \quad (4)$$

$$P = \frac{E \cdot 3600}{\Delta t} \quad (5)$$

C_U is the volumetric capacitance obtained by eqn (2), ΔV is the operating voltage range, and Δt is discharging time. LbL-MWNT/MnO_x MSC exhibits a maximum volumetric energy density of 4.45 mW h cm^{-3} and a maximum volumetric power density of 12.3 W cm^{-3}. These values are higher than those obtained in other all-solid-state supercapacitors using manganese oxide or gel electrolyte.[23,26,31,48,55–57] This result also confirms the excellent performance of our LbL-MWNT/MnO_x MSCs.

It took ~8.2 h for the LbL-MWNT/MnO_x MSC to self-discharge from 0.8 to 0.4 V, as shown in the ESI Fig. S8† and it was observed that the capacitance of the fabricated MSC was decreased when it was kept under ambient-air conditions even without continuous charge–discharge cycles as shown in the ESI Fig. S9.† The observed aging is probably due to the degradation of the PVA–H_3PO_4 gel electrolyte exposed to ambient air. Evaporation of solvent seems to reduce the ionic conductivity of the electrolyte, affecting the adsorption/desorption of ions between the active material and the electrolyte and disturbing the ionic charge transfer. Therefore, systematic investigations on the aging of MSCs are currently being performed.

Next, we fabricated a flexible LbL-MWNT/MnO_x MSC circuit on a 75 μm thick PET film. A flexible MSC circuit is composed of four MSC arrays and connected in series or in parallel to increase the output voltage or total capacitance, where each MSC array consists of 3 × 3 MSCs as shown in Scheme 1.

Fig. 5(a) shows a flexible MSC circuit with 4 MSC arrays connected in series and the corresponding circuit diagram is given in the inset. Fig. 5(b) shows CV curves of 4 MSC arrays connected in series, in parallel, or 2 in series and 2 in parallel. By adjusting the operating voltage and capacity according to the circuit design, the energy of the MSC circuit can be controlled effectively. Four serially connected MSC arrays have an output voltage of 3.2 V, which is four times higher than that of a single MSC array with a voltage of 0.8 V. However, the total capacitance is reduced to a quarter of a single MSC array. In the case of 4 MSC arrays connected in parallel, the voltage is identical to a single MSC array but the total capacitance is increased four times. After fully charging 4 LbL-MWNT/MnO_x MSC arrays connected in series, we could turn on various LEDs operating at different voltages, as demonstrated in the inset of Fig. 5(b).

In order to evaluate the mechanical stability of the fabricated MSC circuit on a PET film with respect to bending, CV curves were measured at various bending radii for both convex and concave bending (Fig. 5(c)). Regardless of the bending radius or the direction of bending, the total area as well as the rectangular shape of the CV curves remained the same at a scan rate of 500 mV s^{-1}. Photographic images of the flexible MSC circuit on

a PET film under various bending conditions are shown in the ESI Fig. S10.† Even after 1000 bending cycles, the capacitance kept its original value, certifying the mechanical stability of the fabricated MSC arrays (Fig. 5(d)).

4. Conclusions

By using LbL-MWNT/MnO_x nanocomposite electrodes in the fabrication of all-solid-state MSCs, we obtained dramatically enhanced performance compared to LbL-MWNT MSCs, characterized by a volumetric capacitance of 50 F cm^{-3} at a scan rate of 10 mV s^{-1}, a high volumetric energy density of 4.45 mW h cm^{-3}, and a power density of 12.3 W cm^{-3}. After 10 000 operation cycles, the capacitance remained at about 88.3% of the original value. By the deliberate circuit design of MSC arrays, the output voltage and the capacitance of the MSC arrays could be controlled, applicable to the operation of various LEDs requiring different voltages. Furthermore, we could fabricate a mechanically stable and flexible MSC circuit on a PET film. This work demonstrates the potential for application of flexible all-solid-state planar-type MSCs in future portable nanoelectronics.

Acknowledgements

This work was supported by the National Research Foundation of Korea (NRF) grant funded by the Korea government (MEST) (grant no. NRF-2013R1A2A1A01016165). We also thank KU-KIST Graduate School Program, Korea.

Notes and references

1 X. Zhang, L. Gong, K. Liu, Y. Cao, X. Xiao, W. Sun, X. Hu, Y. Gao, J. Chen, J. Zhou and Z. L. Wang, *Adv. Mater.*, 2010, **22**, 5292–5296.
2 L. Yuan, X. H. Lu, X. Xiao, T. Zhai, J. Dai, F. Zhang, B. Hu, X. Wang, L. Gong, J. Chen, C. Hu, Y. Tong, J. Zhou and Z. L. Wang, *ACS Nano*, 2012, **6**, 656–661.
3 X. Lu, G. Wang, T. Shai, M. Yu, J. Gan, Y. Tong and Y. Li, *Nano Lett.*, 2012, **12**, 1690–1696.
4 X. Jia, Z. Chen, X. Cui, Y. Peng, X. Wang, G. Wang, F. Wei and Y. Lu, *ACS Nano*, 2012, **6**, 9911–9919.
5 X. Wang, B. Liu, Q. Wang, W. Song, X. Hou, D. Chen, Y. Cheng and G. Shen, *Adv. Mater.*, 2013, **25**, 1479–1486.
6 X. Li, G. Wang, X. Wang, X. Li and J. Ji, *J. Mater. Chem. A*, 2013, **1**, 10103.
7 J. Feng, X. Sun, C. Wu, L. Peng, C. Lin, S. Hu, J. Yang and Y. Xie, *J. Am. Chem. Soc.*, 2011, **133**, 17832–17838.
8 Z. Yan, L. Ma, Y. Zhu, I. Lahiri, M. G. Hahm, Z. Liu, S. Yang, C. Xiang, W. Lu, Z. Peng, Z. Sun, C. Kittrell, J. Lou, W. Choi, P. M. Ajayan and J. M. Tour, *ACS Nano*, 2013, **7**, 58–64.
9 Z. Niu, W. Zhou, J. Chen, G. Feng, H. Li, Y. Hu, W. Ma, H. Dong, J. Li and S. Xie, *Small*, 2013, **9**, 518–524.
10 Y. Yamada, T. Tanaka, K. Machida, S. Suematsu, K. Tamamitsu, H. Kataura and H. Hatori, *Carbon*, 2012, **50**, 1422–1424.
11 Z. Niu, L. Zhang, L. Liu, B. Zhu, H. Dong and X. Chen, *Adv. Mater.*, 2013, **25**, 4035–4042.
12 Z. Niu, H. Dong, B. Zhu, J. Li, H. H. Hng, W. Zhou, X. Chen and S. Xie, *Adv. Mater.*, 2013, **25**, 1058–1064.
13 R. R. Bi, X. L. Wu, F. Cao, L. Y. Jiang, Y. G. Guo and L. J. Wan, *J. Phys. Chem. C*, 2010, **114**, 2448–2451.
14 Z. S. Wu, D. W. Wang, W. Ren, J. Zhao, G. Zhou, F. Li and H. M. Cheng, *Adv. Funct. Mater.*, 2010, **20**, 3595–3602.
15 X. Zhang, W. Shi, J. Zhu, D. J. Khartistal, W. Zhao, B. S. Lalia, H. H. Hng and Q. Yan, *ACS Nano*, 2011, **5**, 2013–2019.
16 D. P. Dubal, G. S. Gund, R. Holze and C. D. Lokhande, *J. Power Sources*, 2013, **242**, 687–698.
17 C. Y. Cao, W. Guo, Z. M. Cui, W. G. Song and W. Cai, *J. Mater. Chem.*, 2011, **21**, 3204.
18 Q. Lu, M. W. Lattanzi, Y. Chen, X. Kou, W. Li, X. Fan, K. M. Unruh, J. G. Chen and J. Q. Xiao, *Angew. Chem.*, 2011, **123**, 6979–6982.
19 W. Chen, R. B. Rakhi, L. Hu, X. Xie and H. N. Alshareef, *Nano Lett.*, 2011, **11**, 5165–5172.
20 H. Gao, F. Xiao, C. B. Ching and H. Duan, *ACS Appl. Mater. Interfaces*, 2012, **4**, 7020–7026.
21 J. Duay, E. Gillette, R. Liu and S. B. Lee, *Phys. Chem. Chem. Phys.*, 2012, **14**, 3329–3337.
22 C. C. Hu, K. H. Chang, M. C. Lin and Y. T. Wu, *Nano Lett.*, 2006, **6**, 2690–2695.
23 W. Si, C. Yan, Y. Chen, S. Oswald, L. Han and O. G. Schmidt, *Energy Environ. Sci.*, 2013, **6**, 3218–3223.
24 J. W. Lee, A. S. Hall, J. D. Kim and T. E. Mallouk, *Chem. Mater.*, 2012, **24**, 1158–1164.
25 J. Ren, L. Li, C. Chen, X. Chen, Z. Cai, L. Qiu, Y. Wang, X. Zhu and H. Peng, *Adv. Mater.*, 2013, **25**, 1155–1159.
26 X. Xiao, T. Li, P. Yang, Y. Gao, H. Jin, W. Ni, W. Zhan, X. Zhang, Y. Cao, J. Zhong, L. Gong, W. C. Yen, W. Mai, J. Chen, K. Huo, Y. L. Chueh, Z. L. Wang and J. Zhou, *ACS Nano*, 2012, **6**, 9200–9206.
27 G. An, P. Yu, M. Xiao, Z. Liu, Z. Miao, K. Ding and L. Mao, *Nanotechnology*, 2008, **19**, 275709.
28 S. W. Lee, J. H. Kim, S. Chen, P. T. Hammond and Y. Shao-Horn, *ACS Nano*, 2010, **4**, 3889–3896.
29 Y. Cheng, S. Lu, H. Zhang, C. V. Varanasi and J. Liu, *Nano Lett.*, 2012, **12**, 4206–4211.
30 L. Hu, W. Chen, X. Xie, N. Liu, Y. Yang, H. Wu, Y. Yao, M. Pasta, H. N. Alshareef and Y. Cui, *ACS Nano*, 2011, **5**, 8904–8913.
31 P. Yang, X. Xiao, Y. Li, Y. Ding, P. Qiang, X. Tan, W. Mai, Z. Lin, W. Wu, T. Li, H. Jin, P. Liu, J. Zhou, C. P. Wong and Z. L. Wang, *ACS Nano*, 2013, **7**, 2617–2626.
32 J. Chmiola, C. Largeot, P. L. Taberna, P. Simon and Y. Gogotsi, *Science*, 2010, **328**, 480–483.
33 L. Peng, X. Peng, B. Liu, C. Wu, Y. Xie and G. Yu, *Nano Lett.*, 2013, **13**, 2151–2157.
34 Y. J. Kang, S. J. Chun, S. S. Lee, B. Y. Kim, J. H. Kim, H. Chung, S. Y. Lee and W. Kim, *ACS Nano*, 2012, **6**, 6400–6406.
35 K. Ariga, J. P. Hill and Q. Ji, *Phys. Chem. Chem. Phys.*, 2007, **9**, 2319–2340.
36 G. Decher, *Science*, 1997, **277**, 1232–1237.
37 S. W. Lee, B. S. Kim, S. Chen, S. H. Yang and P. T. Hammond, *J. Am. Chem. Soc.*, 2009, **131**, 671–679.

38 D. Kim, G. Shin, Y. J. Kang, W. Kim and J. S. Ha, *ACS Nano*, 2013, **7**, 7975–7982.
39 M. Zhang, L. Su and L. Mao, *Carbon*, 2006, **44**, 276–283.
40 M. Toupin, T. Brousse and D. Belanger, *Chem. Mater.*, 2002, **14**, 3946–3952.
41 M. Chigane and M. Ishikawa, *J. Electrochem. Soc.*, 2000, **147**, 2246.
42 A. M. E. Raj, S. G. Victoria, V. B. Jothy, C. Ravidhas, J. Wollschlager, M. Suendorf, M. Neumann, M. Jayachandran and C. Sanjeeviraja, *Appl. Surf. Sci.*, 2010, **256**, 2920.
43 J. Yan, Z. Fan, T. Wei, W. Qian, M. Zhang and F. Wei, *Carbon*, 2010, **48**, 3825–3833.
44 P. L. Taberna, P. Simon and J. F. Fauvarque, *J. Electrochem. Soc.*, 2003, **150**, A292–A300.
45 L. Y. Yuan, X. H. Lu, X. Xiao, T. Zhai, J. J. Dai, F. C. Zhang, B. Hu, X. Wang, L. Gong, J. Chen, C. G. Hu, Y. X. Tong, J. Zhou and Z. L. Wang, *ACS Nano*, 2012, **6**, 656–661.
46 K. Wang, W. J. Zou, B. G. Quan, A. F. Yu, H. P. Wu, P. Jiang and Z. X. Wei, *Adv. Energy Mater.*, 2011, **1**, 1068–1072.
47 C. Portet, G. Yushin and Y. Gogotsi, *Carbon*, 2007, **45**, 2511–2518.
48 D. Pech, M. Brunet, H. Durou, P. H. Huang, V. Mochalin, Y. Gogotsi, P. L. Taberna and P. Simon, *Nat. Nanotechnol.*, 2010, **5**, 651–660.
49 F. Meng and Y. Ding, *Adv. Mater.*, 2011, **23**, 4098–4102.
50 D. Pech, M. Brunet, P. L. Taberna, P. Simon, N. Fabre, F. Mesnilgrente, V. Conédéra and H. Durou, *J. Power Sources*, 2010, **195**, 1266–1269.
51 K. Wang, W. Zou, B. Quan, A. Yu, H. Wu, P. Jiang and Z. Wei, *Adv. Energy Mater.*, 2011, **1**, 1068–1072.
52 K. Sheng, Y. Sun, C. Li, W. Yuan and G. Shi, *Sci. Rep.*, 2012, **2**, 247.
53 C. L. Liu, K. H. Chang, C. C. Hu and W. C. Wen, *J. Power Sources*, 2012, **217**, 184–192.
54 Z. Chen, Y. Qin, D. Weng, Q. Xiao, Y. Peng, X. Wang, H. Li, F. Wei and Y. Lu, *Adv. Funct. Mater.*, 2009, **19**, 3420–3426.
55 X. Lu, M. Yu, G. Wang, T. Zhai, S. Xie, Y. Ling, Y. Tong and Y. Li, *Adv. Mater.*, 2013, **25**, 267–272.
56 M. F. El-Kady, V. Strong, S. Dubin and R. B. Kaner, *Science*, 2012, **335**, 1326–1330.
57 M. F. El-Kady and R. B. Kaner, *Nat. Commun.*, 2013, **4**, 1475.